nature astronomy

Article

https://doi.org/10.1038/s41550-022-01799-5

Determination of X-ray pulsar geometry with IXPE polarimetry

Received: 2 July 2022

Accepted: 31 August 2022

Published online: 24 October 2022

Check for updates

A list of authors and their affiliations appears at the end of the paper

Using observations of X-ray pulsar Hercules X-1 by the Imaging X-ray Polarimetry Explorer we report a highly significant (>17σ) detection of the polarization signal from an accreting neutron star. The observed degree of linear polarization of ~10% is far below theoretical expectations for this object, and stays low throughout the spin cycle of the pulsar. Both the degree and angle of polarization exhibit variability with the pulse phase, allowing us to measure the pulsar spin position angle 57(2) deg and the magnetic obliquity 12(4) deg, which is an essential step towards detailed modelling of the intrinsic emission of X-ray pulsars. Combining our results with the optical polarimetric data, we find that the spin axis of the neutron star and the angular momentum of the binary orbit are misaligned by at least ~20 deg, which is a strong argument in support of the models explaining the stability of the observed superorbital variability with the precession of the neutron star.

X-ray pulsars are strongly magnetized neutron stars powered by accretion from a donor star in binary systems. The strong magnetic field funnels the accreting material to the polar caps of the compact object, where the energy is released producing the observed pulsed emission as the neutron star rotates. Hercules X-1 (Her X-1) is the second X-ray pulsar ever discovered[1], one of the few persistent accretion-powered pulsars in the sky and is arguably the most studied object of its type. Her X-1/HZ Her is an intermediate mass X-ray binary at a distance of ~7 kpc (ref. [2]) consisting of a persistently accreting neutron star with the spin period of ~1.24 s and a B3, ~2.2 solar mass donor star eclipsing the X-ray source approximately every ~1.7 d as they orbit each other in a nearly circular orbit[1,3]. The neutron star has strong magnetic field of 4.5×10^{12} G, and Her X-1 is the first neutron star for which the field was measured directly through the detection of a cyclotron resonance scattering feature in the X-ray spectrum[4]. Besides the spin and orbital variations, surprisingly stable ~35 d superorbital variability is also observed in this system[5]. Flux variability is thought to be related to obscuration of the compact object by the precessing warped accretion disk at certain precession phases, and is accompanied by regular changes in the pulse profiles. The latter fact motivated the hypothesis that a precession of the accretion disk might be clocked by the neutron star precession via some feedback mechanism[6–8].

The X-ray radiation from Her X-1 was anticipated to be strongly polarized with a polarization degree (PD) of up to 60–80% expected in some models[9], so it was chosen as one of the first targets for the Imaging X-ray Polarimetry Explorer (IXPE), a NASA mission in partnership with the Italian space agency (ASI) equipped with detectors sensitive to linear polarization of X-rays in the nominal 2–8 keV band. Here we report the results of these observations and the measurement of the linear polarization from an accreting neutron star. We also discuss how polarimetry can be used to constrain the basic geometry of the pulsar and test the hypothesis of free precession of the neutron star in this binary system. Finally, we discuss the challenges that low observed polarization degree poses for X-ray pulsar emission models.

The source was observed by IXPE on 2022 February 17–24, at the beginning of the 35 d precession cycle, the so-called main-on state, as illustrated in Fig. 1. The observation started while the pulsar was still obscured by the outer edge of the warped and tilted accretion disk[10,11] and continued throughout the first part of the main-on state where the neutron star emerges from behind the accretion disk and becomes visible directly[12]. IXPE had, therefore, a direct and clear view of the neutron star through most of the observation, except for brief periods when the pulsar was eclipsed by the donor star, and the so-called pre-eclipse

e-mail: doroshv@astro.uni-tuebingen.de; juri.poutanen@utu.fi

https://doi.org/10.1038/s41550-022-01799-5

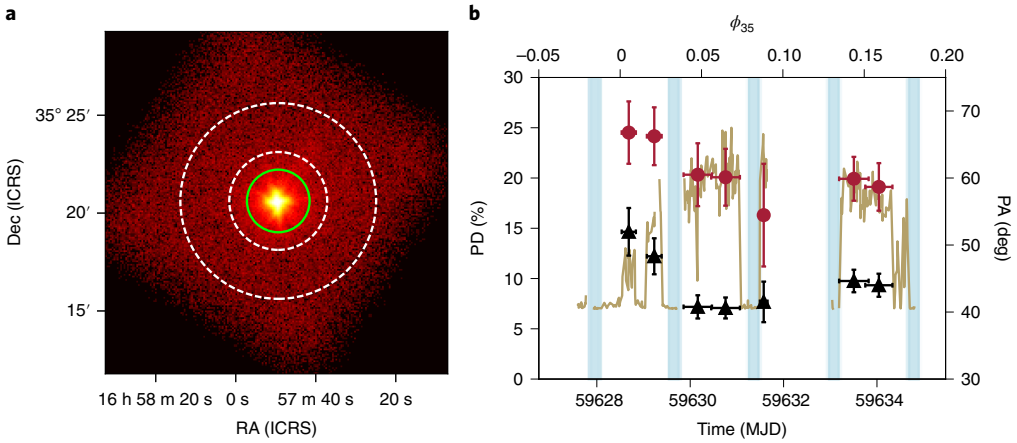

Fig. 1 | Overview and evolution of polarization properties of Her X-1 over the period of observation. a, The source (green circle) and background (area enclosed by white dashed circles) extraction regions are indicated on top of a broadband (2–7 keV) image of Her X-1 observed by IXPE (all three detectors combined, image plotted in International Celestial Reference System (ICRS) coordinates). **b**, Evolution of the observed flux from Her X-1 (brown curve), PD (black triangles, left *y* axis) and PA (red circles, right *y* axis) with time and phase Φ_{35} of the 35 d super-orbital precesession cycle (numerical values are listed in Supplementary Table 3). The turn-on time MJD 59628.5 is estimated from the IXPE data and the superorbital period of 34.85 d is assumed. The reported values and the uncertainties correspond to the mean values and 1σ (68%) confidence intervals. The vertical blue stripes show eclipses by the companion star (eclipses and pre-eclipse dips are excluded from the analysis).

dips, which are associated with obscuration by the outer-disk regions disturbed by the interaction with the accretion stream from the donor star[13] or by the gas stream itself[14]. The data taken during the eclipses of the pulsar and during periods of strong absorption were excluded from the analysis. This resulted in a total effective exposure time of ~150 ks suitable for polarimetric and spectropolarimetric analysis based on the formalism outlined in ref. [15] and ref. [16] and in standard use for all IXPE observations up to now, which is described in detail in the Methods.

Results

We started the analysis by looking at the phase-averaged polarization of the emission from Her X-1, using all photons collected throughout the observation in the broad 2–7 keV energy band, ignoring the 7–8 keV band due a higher background and remaining calibration uncertainties. We detected a highly significant and well-constrained polarization signal, with a polarization degree (PD) of 8.6 ± 0.5% and polarization angle (PA, measured from north to east) of 62°± 2° (all uncertainties are quoted at 1σ confidence levels unless stated otherwise). The measured PD is significantly lower than the predicted 60–80% for the source[9], which raises questions for new theoretical investigations (as we discuss below). We emphasize that the unexpectedly low polarization is clearly intrinsic to the radiation emerging from the pulsar, and cannot be explained by the signal being depolarized on its way from the pulsar to the observer—for example, by scattering in the accretion flow or accretion disk atmosphere. Indeed, as already mentioned, the source is expected to be observed directly throughout most of the observation. Moreover, the PD seems to be minimal at the peak of the main-on state where the flux is maximal, and thus the amount of scattering material minimal, as illustrated in Fig. 1. As the next step, we investigated the dependence of the polarization properties on photon energy. We found that both the PD and PA seem to be independent of energy (Fig. 2 and Extended Data Fig. 1), with only an indication at the ~2σ confidence level (Methods) for the PD increasing towards higher energies. We continue, therefore, to discuss only the energy-averaged polarization properties within the relatively narrow energy band covered by IXPE.

Pulsar geometry can only be constrained through analysis of the pulse-phase dependence of the polarization properties, and we did in fact observe strong and highly significant variations in the polarization properties with the spin phase, as illustrated in Fig. 3. We note that the PD remains well below expectations for all pulse phases, never exceeding ~15%, which is not dramatically higher than the phase-averaged value. The phase dependence of the observed PD is relatively complex, whereas the PA shows simpler, roughly sinusoidal dependence. The observed spin-phase dependence of the PA can be interpreted within the basic assumptions of X-ray pulsar modelling. In fact, photons originating from different parts of the emission region are expected to substantially align with the magnetic field as they propagate in the highly magnetized plasma surrounding the X-ray pulsar. Vacuum birefringence causes the polarized radiation in the magnetosphere to propagate in the normal, ordinary (O) and extraordinary (X) modes, which represent oscillations of the electric field parallel and perpendicular to the plane formed by the local magnetic field and the photon momentum[17,18] and propagation in the normal modes continues within the so-called polarization limiting radius[19]. This radius is estimated to be about thirty stellar radii for typical X-ray pulsars[20], and at such distances the field is expected to be dominated by the dipole component. The polarization measured at the telescope is expected, therefore, to be either parallel or perpendicular to the instantaneous projection of the magnetic dipole axis of the star onto the plane of the sky. In this scenario, the variation of the PA with phase is a purely geometrical effect and therefore is not related to changes in the PD or flux.

On the basis of these considerations, we could constrain the pulsar geometry by modelling the pulse-phase dependence of the PA with the rotating vector model (RVM)[21]. If the position angle (measured from north to east) of the pulsar angular momentum is χ_p and the pulsar radiation is dominated by the ordinary O mode, then the variations of the X-ray PA with the pulsar phase ϕ can be described by the expression [22]

$$\tan(\mathrm{PA} - \chi_p) = \frac{-\sin\theta\,\sin(\phi-\phi_0)}{\sin i_p\,\cos\theta - \cos i_p\,\sin\theta\,\cos(\phi-\phi_0)}, \quad (1)$$

where i_p is the inclination of the neutron star angular momentum to the line of sight (defined in the interval [0°, 180°]), θ is the inclination of the magnetic dipole to the spin axis (that is the magnetic obliquity) and ϕ_0 is the phase of the light curve when the spot is closest to the observer (see Fig. 4 for geometry).

https://doi.org/10.1038/s41550-022-01799-5

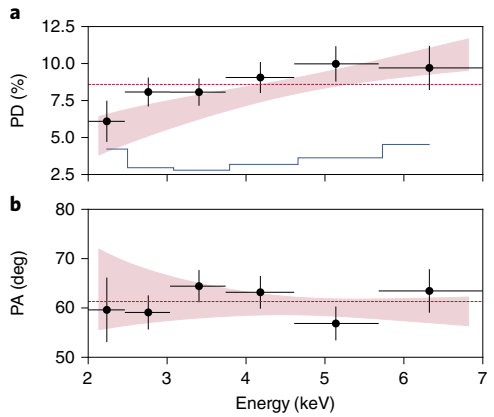

Fig. 2 | Energy dependence of the polarization of Her X-1. a,**b**, The pulse-phase-averaged PD (**a**) and PA (**b**) as a function of photon energy estimated using the formalism of ref. [15] are shown by the black circles. The *y*-axis error bars correspond to 1σ and the *x*-axis error bars reflect the width of the energy bins used for binned analysis. The blue line in **a** shows the estimated minimal detectable polarization at the 99% confidence level for each bin. The shaded regions correspond to the 1σ confidence interval for the spectropolarimetric analysis with the POLPOW model. The dashed horizontal lines indicate average values of the PD (**a**) and PA (**b**) over the full energy band.

Using Bayesian inference code BXA[23], we fitted the PA data from Fig. 3 using RVM with four free parameters (χ_p, θ, i_p and ϕ_0). We assumed flat priors for all parameters: $\chi_p \in [-90°, 90°]$, $\theta \in [0°, 90°]$, $i_p \in [0°, 180°]$ and $\phi_0/(2\pi) \in [-0.5, 0.5]$. The resulting posterior distributions are shown in Fig. 5. The magnetic obliquity and the pulsar position angle were both well constrained: $\theta = 12.1 \pm 3.7°$ and $\chi_p = \chi_{p,*} = 56.9 \pm 1.6°$ (where the asterix subscript corresponds to a solution where the electric vector is parallel to the projection of the rotation axis on the sky). As only the orientation of the polarization plane could be measured, the polarimetric data cannot distinguish between oppositely directed pulsar spins. Therefore, another solution with the oppositely directed spin exists: $\chi_p = \chi_{p,*} \pm 180°$. If radiation escaping from the pulsar is polarized perpendicular to the magnetic field direction (that is, in the X mode), then the position angle of the pulsar spin can have two possible values: $\chi_p = \chi_{p,*} \pm 90° = 146.9° \pm 1.6°$ or $-33.1 \pm 1.6°$, respectively. Other angles (particularly θ) are not affected by the spin direction or uncertainty in the intrinsic polarization of radiation escaping from the surface. We emphasize that the value of θ is in excellent agreement with the indirect estimates obtained from modelling of the observed pulse profile shape[24]. This both lends support to our assumption that the PA at least approximately follows the RVM model, and lends some credibility to the aforementioned modelling of the pulse profile shapes. It is important to highlight that all previous estimates of the magnetic colatitude were based on indirect arguments, whereas our measurement is direct. Finally, we measured the position angle of the pulsar's rotation axis on the sky.

On the other hand, the X-ray polarimetry alone does not allow us to obtain meaningful constraints on the pulsar inclination; our measurement is, however, still fully consistent with the independent estimates of the binary orbit inclination[25]. Indeed, pulsar inclination has a relatively large uncertainty, $i_p = 95° \pm 37°$, with the posterior probability distribution extending from 0° all the way up to 180°, that can be approximated by the function

$$\frac{dp}{di_p} \propto \begin{cases} \sin^{1.5}(90°\, i_p/i_{peak}), & i_p \le i_{peak} \\ \sin^{1.4}[90°\,(2i_{peak} - i_p - 180°)/(i_{peak} - 180°)], & i_p > i_{peak}, \end{cases} \quad (2)$$

where $i_{peak} = 97°$ is the angle where the distribution peaks. This value is consistent with literature estimates for the orbital inclination of $i_{orb} \approx 80$–$90°$ (refs. [26,27]).

Given that free precession of the neutron star has been previously suggested to explain stability of the 35 d precession cycle[6–8,28], it is, however, still interesting to test whether the spin axis of the pulsar and orbital angular momentum are aligned. This can be done despite the fact that inclination of the pulsar with respect to the line of sight is poorly constrained by X-ray polarimetry alone if the orientation of the orbital plane on the sky is known. Such constraints can be obtained from the optical polarimetric observations of Her X-1 over its orbital period[29] assuming that optical polarization results from scattering by an optically thin material corotating with the system, as seen by eRosita[30]. To do that we started by fitting the phase curves of the normalized Stokes parameters digitalized from fig. 1 in ref. [29] with the Fourier series

$$\begin{aligned} q &= q_0 + q_1 \cos\varphi + q_2 \sin\varphi + q_3 \cos 2\varphi + q_4 \sin 2\varphi, \\ u &= u_0 + u_1 \cos\varphi + u_2 \sin\varphi + u_3 \cos 2\varphi + u_4 \sin 2\varphi, \end{aligned} \quad (3)$$

where φ is the orbital phase. If the polarization is produced by Thomson scattering in an optically thin medium corotating with the system, the orbital orientation can be obtained from the Fourier coefficients[31]. The best-fitting Fourier coefficients and their errors obtained by us are given in Supplementary Table 4 and are close to those reported in ref. [29]. These coefficients can be used to derive i_{orb} and the position angle χ_{orb} of the projection of the orbital axis[25,32]:

$$\left(\frac{1-\cos i_{orb}}{1+\cos i_{orb}}\right)^4 = \frac{(u_3+q_4)^2 + (u_4-q_3)^2}{(u_4+q_3)^2 + (u_3-q_4)^2}, \quad (4)$$

$$\tan(2\chi_{orb}) = \frac{A+B}{C+D}, \quad (5)$$

where

$$\begin{aligned} A &= \frac{u_4-q_3}{(1-\cos i_{orb})^2}, \quad B = \frac{u_4+q_3}{(1+\cos i_{orb})^2}, \\ C &= \frac{q_4-u_3}{(1+\cos i_{orb})^2}, \quad D = \frac{u_3+q_4}{(1-\cos i_{orb})^2}. \end{aligned} \quad (6)$$

These formulae give us $i_{orb} = 100.4 \pm 4.9°$ and $\chi_{orb} = \chi_{orb,*} = 28.9 \pm 5.9°$ (or $\chi_{orb} = \chi_{orb,*} - 180° = -151.1° \pm 5.9°$, which is equally acceptable as only the orientation of the polarization plane can be measured). The final values for all geometrical parameters of the system, including constraints from X-ray and optical polarimetry, are summarized in Table 1. The obtained orbital inclination is larger than 90°, which might seem to be at odds with independent inclination estimates quoted above. We note, however, that these estimates are based on modelling of the donor star radius from optical spectroscopy and X-ray eclipses, and cannot distinguish between clockwise and anticlockwise rotation (that is, between inclinations $i_{orb} < 90°$ and $180° - i_{orb}$). In particular, the estimates listed in table 8 of ref. [27] seem to favour inclinations in the range $i_{orb} \approx 80$–$83°$ or $180° - i_{orb} \approx 97$–$100°$ for a distance range of 6.5–7.5 kpc, estimated from Gaia EDR3 data[2]. This implies that our estimate is fully consistent with the literature values, and that the binary is rotating clockwise on the sky. We emphasize that result can only be obtained from polarimetry—in this case, in the optical band.

Using constraints on the 3D orientation of the pulsar and the orbit, we could then obtain the misalignment angle β between the pulsar and the orbital angular momenta:

$$\cos\beta = \cos i_p \cos i_{orb} + \sin i_p \sin i_{orb} \cos\Delta, \quad (7)$$

https://doi.org/10.1038/s41550-022-01799-5

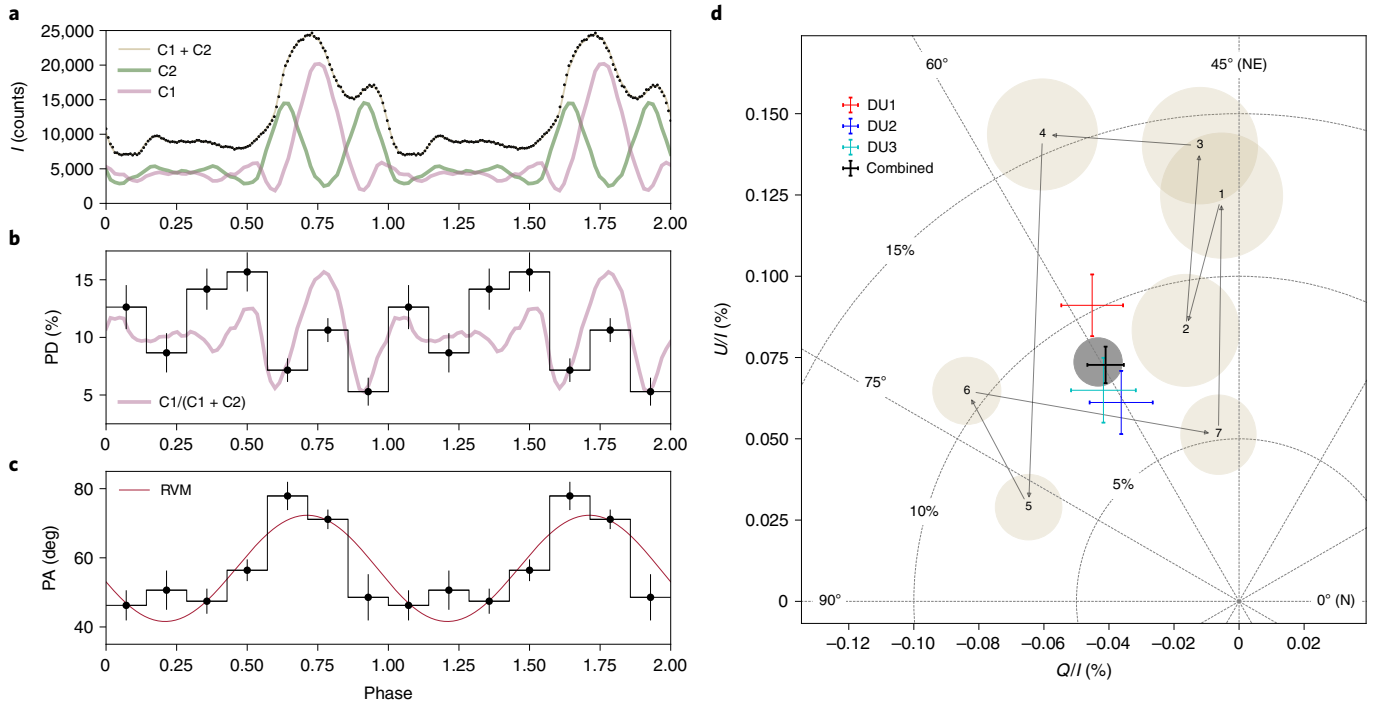

Fig. 3 | Pulse-phase dependence of the polarization properties of Her X-1. **a**, The observed pulse profile in the 2–7 keV energy range (intensity I, in units of counts per 1/128 phase interval) and its decomposition into single-pole pulse profiles labelled C1 and C2[24]. **b**,**c**, The PD (**b**) and PA (**c**) estimated from the spectropolarimetric fit are shown as a function of pulse phase with black circles. The purple line in **b** shows the relative contributions of the main pole (C1, which dominates the main peak) to the total flux, and the red line in **c** shows the best-fitting approximation for the PA with the rotating vector model. **d**, The normalized Stokes parameters Q/I and U/I are shown for each phase bin with brown ellipses representing the 1σ confidence regions for the Stokes parameters (numbers indicate sequential bin number in **a** and **b** from left to right). The black shaded circle shows the Stokes parameters for the pulse-phase-averaged analysis based on the spectropolarimetric fit. The results for the unbinned analysis[15] for individual detector units and the three detectors combined are shown by coloured error bars. Points correspond to the mean values and the error bars correspond to 1σ confidence levels.

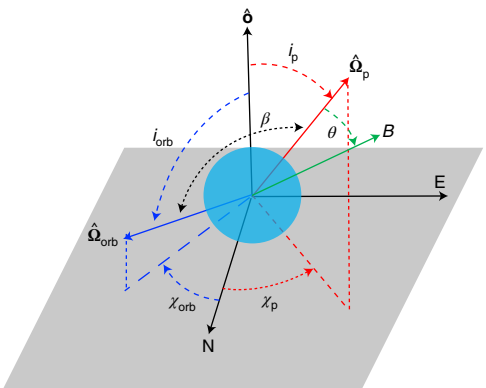

Fig. 4 | Geometry of the system from the observer's perspective. The grey plane is the plane of the sky, labelled with north and east axes, perpendicular to the line of sight towards the observer $\hat{\mathbf{o}}$. The angles between the line of sight and the vectors of the pulsar spin $\hat{\Omega}_p$ and the orbital angular momentum $\hat{\Omega}_{orb}$ are the inclinations i_{orb} and i_p. The corresponding position angles χ_p and χ_{orb} are the azimuthal angles of the spin vectors projected onto the sky, measured from north to east. The misalignment angle β is defined as the angle between $\hat{\Omega}_p$ and $\hat{\Omega}_{orb}$. The magnetic obliquity θ is the angle between magnetic dipole and the rotational axis.

where $\Delta = \chi_p - \chi_{orb}$ is the difference between the position angles of the pulsar spin vector and the orbital angular momentum (the geometry is illustrated in Fig. 4). The parameters we use are given in Table 1. Assuming normal distributions for χ_p and χ_{orb} with the corresponding 1σ errors obtained above, a normal distribution for i_{orb} from the optical polarimetry and the posterior distribution for i_p given by equation (2), we performed Monte Carlo simulations to obtain a probability distribution for β, which is shown in Extended Data Fig. 2 and listed in Supplementary Table 5. For radiation in the O mode (when $\chi_p = \chi_{p,*} = 56.9 \pm 1.6°$ and taking $\chi_{orb} = 28.9 \pm 5.9°$), we obtained the smallest misalignment β with the distribution peaking at ~30° and a lower limit ~20° at the 90% confidence level (Extended Data Fig. 2a). If $\chi_p = \chi_{p,*} \pm 180°$ (or $\chi_{orb} = \chi_{orb,*} \pm 180°$), the misalignment is much larger, with β peaking at 145° (Extended Data Fig. 2b). For the X-mode polarization, $\chi_p = \chi_{p,*} \pm 90°$, β peaks at ~115° or ~65° (Extended Data Fig. 2c,d). These results are essentially unaffected by the exact form of the distribution of i_p and imply that the spin axis of the neutron star during the observation is inclined with respect to the orbital spin by at least 20°, and possibly by as much as ~160° (Extended Data Fig. 2). We note that low angular momentum of the neutron star implies that accretion torques are expected to align its spin with the orbital angular momentum on a relatively short timescale[33,34], so naively one could expect spin of the pulsar and orbital angular momentum to be aligned. This is, however, apparently not the case.

Discussion

Meaningful interpretation of the observed variation of the PD with pulse phase is only possible if the spectra, the pulse profiles and, now, the observed polarization properties of X-ray pulsars are consistently explained. The observed low degree of polarization in Her X-1 came as a surprise and is inconsistent with predictions, and therefore cannot be interpreted in the framework of existing models. One could imagine, however, several potential scenarios to explain the observed low PD.

https://doi.org/10.1038/s41550-022-01799-5

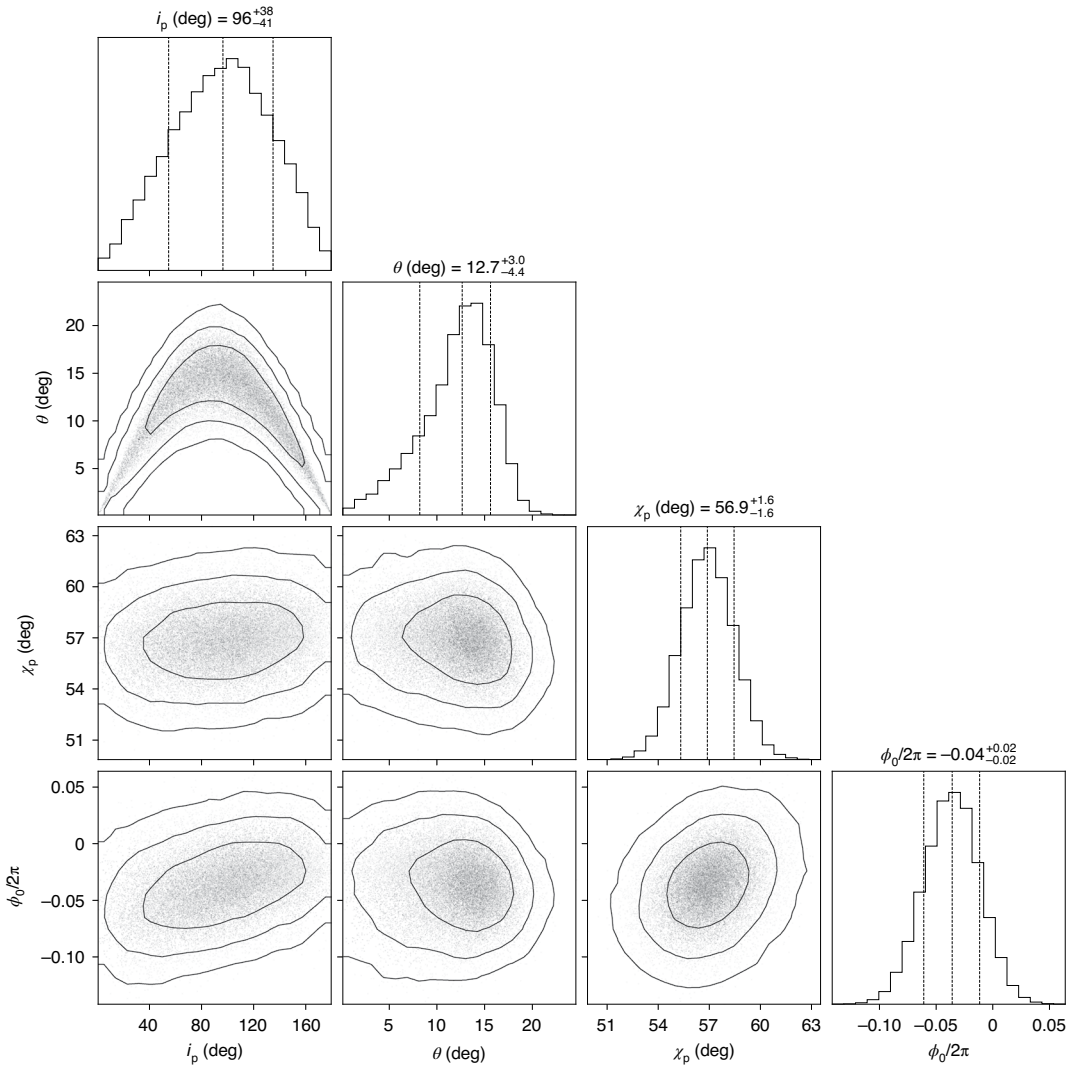

Fig. 5 | Posterior distribution corner plot for the RVM fit of the PA phase dependence. The contours correspond to two-dimensional 1, 2 and 3σ confidence levels derived from the posterior samples shown with the points. The histograms show normalized one-dimensional distribution of a given parameter derived from the posterior samples. The 1σ confidence interval and mean value are indicated in the title and by dashed vertical lines.

For instance, radiative transfer in the magnetized plasma within the emission region with the specific temperature structure of the neutron star atmosphere could be responsible for the observed low PD (Methods). Propagation of the initially polarized X-rays through the magnetosphere could also result in depolarization due to quantum electrodynamical effects[35]. In either scenario, averaging over wider pulse phase intervals or over energy could be expected to reduce the observed PD. Finally, we probably observe emission from both poles of the neutron star combined in least at some pulse phases[24]. Each of the poles could have different polarization properties as both are observed from different angles at any given pulse phase, and mixing the two could therefore reduce the observed PD (Supplementary Fig. 2c). Indeed, modelling of the evolution of the complex observed pulse profile shape over the 35 d cycle[8] suggests multiple emission regions that are probably related to the non-dipolar structure of the magnetic field close to the surface of the neutron star[8,36]. We note that there is an apparent connection between the observed variations and the estimated relative contribution of the pole dominating the main peak of the pulse[24], as illustrated in Fig. 3b. This might suggest that mixing of the emission from different poles might be at least partly responsible for the observed low PD, and it also suggests that the decomposition of the observed pulse profile to single pole components obtained by ref. [24] is probably not far from reality. However, the PD remains low even during the peak where emission is dominated by a single pole. The contribution of the two poles is thus not the only reason for the observed low PD, and it is likely that a combination of several mechanisms is at work. In general, it is clear that a full interpretation of the observed polarization properties of Her X-1 (and other X-ray pulsars), and a full assessment on the scenarios outlined above, requires a deeper understanding of the accretion physics and the emission mechanisms in these objects. This includes the pulse shape, the broadband energy spectrum and its variations with spin and precession phase, the periodic and secular variations in its cyclotron absorption feature and, of course, the polarization properties. So far no theoretical model has explained all these observables, particularly polarization. The observed low PD, therefore, already puts strong constraints on the possible emission mechanisms at play in accretion-powered pulsars, and constitutes a valuable input for theoretical modelling of the emission from accreting magnetized neutron stars.

The polarimetric observations reported here also provide previously unavailable information on the geometry of the source, particularly basic information on the orientation of the pulsar geometry

Table 1 | Orbital and pulsar geometrical parameters of Her X-1

$\chi_{p,*}$	θ	i_p	$\chi_{orb,*}$	i_{orb}
deg	deg	deg	deg	deg
56.9±1.6	12.1±3.7	Eq. (2)	28.9±5.9	100.4±4.9

including the magnetic colatitude and orientation with respect to observer and to the orbit of the binary system. In particular, we find evidence of a misalignment between the spin axis of the pulsar and the orbital angular momentum. The reason for the observed misalignment is unclear, but it could be associated, for instance, with extra torques imposed on the neutron star by the warped accretion disk or free precession of the neutron star[8]. In the latter case in particular the interaction of the inner disk regions with the magnetosphere of a precessing neutron star can greatly diminish (or completely stop) secular spin–orbital alignment[8]. We note that expected alignment was one of the key arguments[33] against a free precession model, and IXPE results invalidate it. It is clear that for a precessing neutron star one can anticipate evolution of the magnetic obliquity θ with the phase of the 35 d cycle[6] resulting in variation of the amplitude of the PA variations with the spin phase. Current observations only cover a small fraction of the 35 d cycle and do not allow us to test this hypothesis. Deeper observations covering a larger fraction of the cycle would be required to characterize this variability quantitatively and unambiguously prove the hypothesis of neutron star precession in this system. Furthermore, new high-precision optical polarimetric observations covering different phases of the superorbital cycle would be useful to confirm the orbital orientation. Nevertheless, the obtained constraints on misalignment of the pulsar spin with the orbital angular momentum represent strong support for the hypothesis of neutron star precession in the system. This information can only be obtained by means of polarimetric observations now also accessible in the X-ray band. Our results illustrate the power of X-ray polarimetry for studies of accreting neutron stars, and offer a new perspective on these long-known, yet still mysterious, objects.

Methods

Analysis of IXPE data

IXPE includes three co-aligned X-ray telescopes, each comprising an X-ray mirror assembly (provided by NASA) and linear-polarization-sensitive pixelated gas pixel detectors (provided by the ASI) to provide imaging polarimetry over a nominal 2–8 keV band. Complete descriptions of the hardware and its performance are given in refs. [37–39]. The gas pixel detectors are, in essence, pixelated proportional counters, which allow us to recover the direction for each primary photoelectron ejected following the interaction of an incident photon with the detector medium. This direction and the track length carry information about the direction of electromagnetic field oscillation associated with each individual photon, and thus can be used to recover polarization properties (that is, the Stokes parameters) for an astrophysical source through analysis of the distribution of track directions for all photons from the source. The amplitude of variation of the track angles for a 100% polarized source is described by the energy-dependent modulation factor. The values and energy dependence of the modulation factor were calibrated both on the ground and continuously monitored in space, and they were taken into account when modelling the polarization as described below.

IXPE data telemetered to the ground stations in Malindi (primary) and Singapore (secondary) are transmitted to the Mission Operations Center at the Laboratory for Atmospheric and Space Physics (University of Colorado) and then to the Science Operations Center at the NASA Marshall Space Flight Center. Using software developed jointly by NASA and the ASI, the Science Operations Center processes science and relevant engineering and ancillary data to produce the data products that are archived at the High-Energy Astrophysics Science Archive Research Center (HEASARC) at the NASA Goddard Space Flight Center for use by the international astrophysics community. IXPE data are distributed in a lower-level format (L1), in which relevant information about event tracks are reported, and also in a higher-level format (L2), in which several corrections have been applied and only the main properties of the reconstructed events are reported. In particular, in the L2 format the photon energy is obtained after corrections for temperature and gain effects. Further corrections for the gain effects are applied using the data from the onboard calibration sources acquired during the observation. The imaging information in L2 is obtained from the L1 data after correcting for dithering of the spacecraft pointing and orbital thermally induced motion of the boom that separates the optics from the detectors. The L2 data were then screened and processed using the HEASOFT version 6.30 software and current calibration files available from https://heasarc.gsfc.nasa.gov.

The data reduction consists of the following main steps. The track images are first processed to separate the signal from electronic noise and then a custom algorithm is applied to derive the characteristics of the event (that is, the direction of the photoelectron emission, the energy, the arrival time and the direction of the incoming photon). The subsequent steps calibrate both the energy and the response to polarization, and filter events flagged as not suitable for further analysis and time intervals in which the source was occulted by the Earth or there were pointing inaccuracies, and so on.

After initial processing, various selection criteria may be imposed for detected photons. These can include the energy (to study the energy dependence of the polarization properties), the arrival time, the pulse or orbital phase, or the position on the detector (to study the spatial dependence of the polarization properties in extended sources or to discriminate between source and background photons for point sources). On the selected event ensemble, the last step is to normalize the measured response to polarization by the modulation factor.

Analysis of polarization is carried out with two different approaches. The first, based on the unbinned formalism presented in ref. [40], is implemented in the IXPE collaboration software suite IXPEOBSSIM version 28.4.0 (ref. [41]). The other method relies on the procedure presented in ref. [16], and is based on the generation of the Stokes spectra, which are then fitted with standard spectral-fitting software, such as XSPEC[42] (here version 12.12.1 is used). The proper instrument response functions are provided by the IXPE team as a part of the IXPE calibration database released on 14 March 2022 and available at HEASARC archive (https://heasarc.gsfc.nasa.gov). All values reported below are based on the spectropolarimetric fits of the Stokes spectra unless otherwise stated. The uncertainties were estimated using a Markov chain Monte Carlo method for respective parameter from spectropolarimetric fits.

Pulse-phase-averaged analysis. As a first step, we investigated the time-averaged polarization from the pulsar. The Stokes parameters were obtained from the L1 data using the unbinned approach of ref. [40] and the spurious modulation was removed following the approach of ref. [43]. The Stokes parameters in the L2 data were distributed with weights obtained following the procedure from ref. [44], which can be used to perform a weighted analysis improving the sensitivity for faint sources. Considering the low background level and the high number of source counts in the case of Her X-1, we did not use the weighted approach for the final results reported. However, we did perform both weighted and unweighted analyses and found compatible results.

The source and background photons were extracted from circular (radius of 1.6′) and annular (with inner and outer radii of 2.5′ and 5′, respectively) regions centred on the source. The extraction radii were chosen to select the source with a proper margin; the background was later removed by subtracting its Stokes parameters, rescaled for the

appropriate extraction area, from those of the source. The average values of the Stokes parameters, and corresponding PD and polarization angle PA, were then estimated in a single 2–7 keV energy band and in four sub-bins covering the same energy range. Note that we conservatively ignored energies in the 7–8 keV energy range to avoid potential systematic effects associated with the remaining energy scale uncertainties (which can be expected to have largest effect around the energies where effective area drops abruptly; that is, around 8 keV) and uncertainties in the alignment of the optical axis at this stage of the mission, which affected the vignetting correction (which is again strongest at the highest energies). We emphasize, however, that these effects mostly affected spectral analysis (that is, the best-fitting parameters of the spectral model) and the polarimetric results were not affected.

In addition to the binned analysis, we also conducted spectropolarimetric modelling of the same dataset. In particular, the Stokes spectra were extracted for each detector unit and modelled simultaneously using absorbed NTHCOMP model[45] for intensity spectra in combination with either the POLCONST or POLPOW polarimetric models. The NTHCOMP model describes a Comptonized spectrum from seed blackbody photons of a characteristic temperature $T_{\rm bb,comp}$ (defining the low energy rollover) by electrons with temperature $T_{\rm e,comp}$ (defining the high energy rollover). Instead of the Thomson optical depth, this model is parameterized by the power law index $\Gamma_{\rm comp}$, because the Comptonized spectrum for non-relativistic electron temperatures is well described by a power law between the photon seed energies and the cutoff energy related to the electron temperature. This model is often used to describe the spectra of X-ray pulsars. The model normalization at 1 keV, $A_{\rm comp}$, and cross-normalization constants defining relative normalization of IXPE detector units two and three relative to the first unit, $C_{\rm DU2}$ and $C_{\rm DU3}$, were also considered as free parameters.

We emphasize that NTHCOMP is a purely phenomenological model and physical interpretation of the best-fitting values is not trivial, as the model is not actually designed to describe the spectra of X-ray pulsars. The spectrum of Her X-1 is known to be more complex than that given by this model (for example, there is a blackbody-like component with $kT \approx 0.1$–0.3 keV and a cyclotron absorption line), but within the IXPE band the spectrum is well described by this simplified model. In fact, the phase-averaged spectrum can even be approximated with a single power law, but this does not apply to all phase bins, hence our choice of the next simplest model. We verified, however, that the choice of the intensity continuum model did not affect any of the polarimetric measurements (as is also justified by the agreement between the binned analysis and the results of the spectropolarimetric analysis.

It is worth noting that at the time of the Her X-1 observation, the IXPE telescope axes were slightly offset with respect to the pointing direction, and that there were uncertainties in modelling of the boom motion during the observation. This caused an additional vignetting with an impact on the effective area calibration, and then on the spectral analysis. However, this had no impact on the measured dependence of the polarization on energy because the polarization was estimated after normalization of the Stokes parameters U and Q to the source flux, which cancels out the systematics related to the effective area. This was also confirmed by the analysis presented in Fig. 1, Extended Data Fig. 1 and Supplementary Table 1. We highlight here the good agreement between the individual detectors and the two independent modelling approaches.

The polarization properties seem to be only weakly dependent on energy, although there is an indication of increase in the PD with energy. Although there seems to be a systematic increase in the PD towards higher energies, and the value of the Pearson correlation coefficient between the PD and energy of ~0.86 suggests a moderate degree of correlation, the values in individual bins (except the first one) are consistent with the average value, as illustrated in Fig. 2. An alternative approach to assess the significance of such an energy dependence is to compare the results of the spectropolarimetric fits for models when polarization is assumed constant to those where it is energy-dependent, which are summarized in Supplementary Table 1. The model where constant polarization was assumed yielded slightly worse fit statistics, but a lower Bayesian information criterion score[46], which makes it statistically preferred. A similar conclusion can be drawn on the basis of the estimated significance of the deviation of the power law index, characterizing the PD dependence on energy $\mathrm{PD}(E) \propto E^{-\Gamma_{\rm PD}}$, from zero, which is estimated at $\Gamma_{\rm PD} = -0.46 \pm 0.20$. It deviates from zero at a confidence level of only ~98%; that is, at ~2σ. The power law index characterizing the dependence of the PA is estimated as $\Gamma_{\rm PA} = 0.04 \pm 0.10$, which is consistent with zero. We conclude, therefore, that there is no strong dependence of the polarization properties on energy, although there is an indication that the PD might actually increase with energy.

Pulse-phase and time-resolved analysis. To investigate the polarization properties as a function of the spin phase, we obtained a timing solution for the pulsar. As a first step, the arrival times of all events were corrected to the Solar System barycentre reference frame using the barycorr task, and then corrected for the effects of motion within a binary system using ephemerides by ref. [47]. A Lomb–Scargle[48,49] periodogram was then constructed to estimate the approximate value of the spin period and to obtain a template pulse profile, which was used to estimate the residual phase delays and the pulse arrival times for observation segments by cross-correlation with the template (we considered continuous segments separated by gaps of at least 1 ks as independent). The obtained pulse arrival times t_n were then used to obtain the final estimate of the spin period $p_{\rm spin} = 1.2377093(2)$ s using the phase connection technique. We found that the observed arrival times were fully consistent with a constant period; that is, $t_n = t_0 + n \times p_{\rm spin}$ as illustrated in Supplementary Fig. 1. It is important to emphasize that no appreciable evolution of the pulse profile shape occurred during the observation, as illustrated in Supplementary Fig. 1 and expected on the basis of previous observations of the source at a similar phase of the precession cycle[50]. This allowed us to use all of the available data and achieve a sufficient sensitivity in the individual phase bins. The observed pulsed fraction in the 2–7 keV band, defined through the maximum and minimum fluxes as $f = (F_{\rm max} - F_{\rm min})/(F_{\rm max} + F_{\rm min})$, is ~55%.

On the basis of the available counting statistics and known instrument sensitivity, seven phase bins were then defined (as shown in Fig. 3). The Stokes spectra ($I/Q/U$), and binned polarization cubes, were then extracted individually for each of the phase bins using IXPEOBSSIM[41]. The background was assumed to be constant for all bins (which is justified as minor variations of the background rate during the observations were averaged out when folded with the spin period of the source). We therefore used Stokes spectra extracted for the entire observation as a background estimate in the phase-resolved analysis (after accounting for differences in the exposure). The extracted spectra were then modelled with the same model as the pulse-phase-averaged spectra to derive the PD and PA using the polconst model. The final values and uncertainties were estimated on the basis of Markov chain Monte Carlo chains produced using the chain command in XSPEC and are reported in Supplementary Table 2. We verified the consistency of the spectropolarimetric and binned analysis results for all bins and found no statistically significant differences in the phase dependence of the PD and PA, therefore only the results of the spectropolarimetric analysis are reported.

The same procedure was used to investigate the time dependence of the polarization properties over the observation. The full dataset was split into seven intervals separated by large gaps defined either by the instrumental good time intervals or by the eclipses of the source. For each interval, the Stokes spectra ($I/Q/U$) were extracted and jointly

modelled using NTHCOMP and POLCONST models to estimate the PD and PA values. The value of the power law index in the NTHCOMP model was considered as a free parameter to accommodate possible minor changes in the spectral shape over the observation. The final values and uncertainties were estimated on the basis of Markov chain Monte Carlo chains produced using the chain command in XSPEC and are reported in Supplementary Table 3. Again, we verified the consistency of the spectropolarimetric and the binned analysis results for all bins and found no significant differences in the phase dependence of the PD and PA, therefore again only results of the spectropolarimetric analysis are reported.

Modelling polarization from a heated neutron star atmosphere

Polarization from a strongly magnetized accreting neutron star is largely defined by the structure of the emission region, which is not known. Earlier estimates for Her X-1[9] were based on the accretion column model[51], which seems to be consistent with the observed broadband spectrum. The observed polarization, however, is substantially lower (~5–15%) than the predicted polarization (60–80%), requiring modifications to the models. There are several mechanisms that may depolarize radiation as it leaves the accretion column and travels through the magnetosphere. For instance, the depolarization can be caused by radiation from the accretion column passing through the so-called vacuum resonance, where the contributions of plasma and magnetized vacuum to the dielectric tensor cancel each other out and fast transformation of the normal modes of radiation occurs[17,18]. If the place where the final scattering of radiation takes place (that is, the photosphere) also lies in this region, we expect substantial Faraday depolarization, reducing the PD without changing the spectral energy distribution or the pulse profile. Furthermore, as the radiation travels from the column through the magnetosphere, it will generally pass through a region where the direction of propagation is nearly parallel to the magnetic field lines. Depending on the geometry of the emission region and the photon energy, this can also result in substantial depolarization[35].

On the other hand, it is unclear whether an accretion column is present at all in Her X-1. Although the observed luminosity is close to the critical value[52], the source demonstrates a positive correlation of the cyclotron line energy with luminosity[53]. This implies that the accreting pulsar is in a sub-critical state where the energy of the infalling matter is dissipated at the neutron star surface but not in a radiation-dominated shock above it. In such a situation, fast ions of the accretion flow heat the neutron star atmosphere, and the thermal photons emerging from this heated atmosphere backscatter on the infalling electrons of the accretion flow with a corresponding energy gain (bulk Comptonization), and these backscattered photons also heat the upper atmosphere. If the local mass accretion rate is close to the critical value, almost all the emergent photons will be backscattered and, as a result, radiation escapes primarily along the tangential direction to the neutron star surface, forming a 'fan'-like angular distribution of the escaping radiation that helps to explain the observed high pulsed fraction. An accurate self-consistent numerical model describing the processes above is yet to be developed. Here we consider a toy model of the overheated magnetized model atmosphere to demonstrate how the observed low polarization can be produced. Such models have been used for interpretation of accreting neutron stars[54–57], although it is important to emphasize that the broadband spectrum of Her X-1 is not well described by any of these models alone.

In this simplified picture, the key process that is responsible for low polarization is a mode conversion at the vacuum resonance. For a given photon energy and magnetic field strength, the vacuum resonance occurs at a plasma density[18] of $\rho_{\rm V} \approx 10^{-4}(B/10^{12}{\rm G})^2 E^2_{\rm keV}\,{\rm g\,cm^{-3}}$. At that density, the contribution of the virtual electron–positron pairs to the dielectric tensor becomes equal to the plasma contribution, and the O and X modes of radiation can convert to each other. Here we consider the radiation transfer in magnetized plasma in the approximation of these two modes, instead of the full description in terms of Stokes parameters. We found that the modes become close to each other at a given photon energy in the emergent spectrum if the vacuum resonance is located in the transition atmospheric layer with a strong temperature gradient from the upper overheated layer of a temperature a few tens of kiloelectronvolts to the lower layer of the atmosphere where the temperature is about 1–2 keV.

We illustrate this statement with a toy model of the transition region between two atmospheric parts (Supplementary Fig. 2a). We assumed a surface magnetic field strength $B = 4 \times 10^{12}$ G, temperature of the overheated layers $T_{\rm up} = 3.1 \times 10^8$ K, and temperature of the bottom cold atmosphere $T_{\rm low} = 1.5 \times 10^7$ K. We considered three different transition depths of $m_{\rm up} = 0.3$, 3 and 30 g cm^{-2}. The corresponding gas pressure was determined by the product of the column density of plasma m and the surface gravity g, $P_{\rm gas} = gm$, computed using the neutron star mass $M = 1.4$ solar masses and radius $R = 12$ km. For the temperature structure, we adopted the dependence

$$T(m) = \frac{T_{\rm up} - T_{\rm low}}{\exp[6(m/m_{\rm up} - 1)] + 1} + T_{\rm low}. \quad (8)$$

We solved the radiation transfer equation for the two modes using the magnetic opacities and the mode conversion as described in ref. [58], with no external radiation flux as the upper boundary condition and the Planck function for the intensity as the lower boundary condition[59]. The polarization fraction of the emergent flux in the observed energy band with and without mode conversion is shown in Supplementary Fig. 2b. The model with the transition depth $m_{\rm up} = 3$ g cm^{-2} demonstrated a low polarization, which is explained by the mode conversion at the transition region with the strong temperature gradient (Supplementary Fig. 3). We note that models with either thinner or thicker overheated layers yielded a higher polarization degree (that is, a larger fraction of total flux is in one of the modes); however, the dominant modes were different in these cases (Supplementary Fig. 2b). If the thickness of the upper layer was low, $m_{\rm up} = 0.3$ g cm^{-2}, the vacuum resonance occurred in the cold, inner part of the atmosphere with strong mode conversion. As a result, the O mode dominated. On the other hand, the mode conversion was inefficient if the vacuum resonance occurred within the overheated layer with $m_{\rm up} = 30$ g cm^{-2}, so the X mode dominated. Note that a depth of the transition layer of $m_{\rm up} \approx 3$ g cm^{-2} seems to be natural as it corresponds to the optical depth of around unity, where free–free cooling becomes inefficient while Compton cooling becomes important. The radiation escaping the atmosphere can be dominated by the O or X modes, depending on the exact value of $m_{\rm up}$ and the detailed temperature structure. The polarization mode can also depend on the angle between the surface normal and the direction of photon propagation. At energies a factor of 10 below the electron cyclotron energy, the vacuum polarization dominates at the outer overheated layer. As a result, both modes are nearly linearly polarized at zenith angles larger than ~6° and therefore over a broad angle range the PD can be computed as the ratio of the difference in the intensities of the two modes to their sum[60]. As an illustration, we show in Supplementary Fig. 2c the PD as observed at different zenith angles for $m_{\rm up} = 3$ g cm^{-2}. We see that at very small and very large inclinations the PD is negative (that is, the X mode dominates), whereas at intermediate angles the PD is positive (that is, the O mode dominates). This indicates that mixing of radiation observed from different emission regions (that is, seen at different zenith angles) can lead to depolarization. We cannot confidently state that the suggested process is responsible for the low polarization of the observed radiation from Her X-1, but it could be important for a final accurate model and for interpretation of the low polarization signal from other X-ray sources, such as magnetars.

Data availability

IXPE data and analysis tools are publicly available from the HEASARC data archive (https://heasarc.gsfc.nasa.gov). Optical polarimetry data used in the paper are published in ref. [29].

References

1. Tananbaum, H. et al. Discovery of a periodic pulsating binary X-ray source in Hercules from UHURU. *Astrophys. J. Lett.* **174**, L143 (1972).
2. Bailer-Jones, C. A. L., Rybizki, J., Fouesneau, M., Demleitner, M. & Andrae, R. Estimating distances from parallaxes. V. Geometric and photogeometric distances to 1.47 billion stars in Gaia Early Data Release 3. *Astron. J.* **161**, 147 (2021).
3. Middleditch, J. & Nelson, J. Studies of optical pulsations from HZ Herculis/Hercules X-1: a determination of the mass of the neutron star. *Astrophys. J.* **208**, 567–586 (1976).
4. Truemper, J. et al. Evidence for strong cyclotron line emission in the hard X-ray spectrum of Hercules X-1. *Astrophys. J. Lett.* **219**, L105–L110 (1978).
5. Giacconi, R. et al. Further X-ray observations of Hercules X-1 from Uhuru. *Astrophys. J.* **184**, 227 (1973).
6. Truemper, J., Kahabka, P., Oegelman, H., Pietsch, W. & Voges, W. EXOSAT observations of the 35 day cycle of Hercules X-1: evidence for neutron star precession. *Astrophys. J. Lett.* **300**, L63 (1986).
7. Staubert, R. et al. Two ~35 day clocks in Hercules X-1: evidence for neutron star free precession. *Astron. Astrophys.* **494**, 1025–1030 (2009).
8. Postnov, K. et al. Variable neutron star free precession in Hercules X-1 from evolution of RXTE X-ray pulse profiles with phase of the 35-d cycle. *Mon. Not. R. Astron. Soc.* **435**, 1147–1164 (2013).
9. Caiazzo, I. & Heyl, J. Polarization of accreting X-ray pulsars - II. Hercules X-1. *Mon. Not. R. Astron. Soc.* **501**, 129–136 (2021).
10. Leahy, D. A. Modelling the extreme ultraviolet emission during the low state of Hercules X-1. *Mon. Not. R. Astron. Soc.* **342**, 446–452 (2003).
11. Klochkov, D. K. et al. Observational manifestations of the change in the tilt of the accretion disc to the orbital plane in Her X-1/HZ Her with phase of its 35-day period. *Astron. Lett.* **32**, 804–815 (2006).
12. Leahy, D. & Wang, Y. The 35-day cycle of Hercules X-1 in multiple energy bands from MAXI and Swift/BAT monitoring. *Universe* **7**, 160 (2021).
13. Igna, C. D. & Leahy, D. A. Light-curve dip production through accretion stream-accretion disc impact in the HZ Her/Her X-1 binary star system. *Mon. Not. R. Astron. Soc.* **425**, 8–20 (2012).
14. Shakura, N. I., Prokhorov, M. E., Postnov, K. A. & Ketsaris, N. A. On the origin of X-ray dips in Her X-1. *Astron. Astrophys.* **348**, 917–923 (1999).
15. Kislat, F., Beilicke, M., Guo, Q., Zajczyk, A. & Krawczynski, H. An unfolding method for X-ray spectro-polarimetry. *Astropart. Phys.* **64**, 40–48 (2015).
16. Strohmayer, T. E. X-ray spectro-polarimetry with photoelectric polarimeters. *Astrophys. J.* **838**, 72 (2017).
17. Gnedin, Y. N., Pavlov, G. G. & Shibanov, Y. A. The effect of vacuum birefringence in a magnetic field on the polarization and beaming of X-ray pulsars. *Sov. Astron. Lett.* **4**, 117–119 (1978).
18. Pavlov, G. G. & Shibanov, Y. A. Influence of vacuum polarization by a magnetic field on the propagation of electromagnetic waves in a plasma. *Sov. J. Exp. Theor. Phys.* **49**, 741–749 (1979).
19. Heyl, J. S. & Shaviv, N. J. Polarization evolution in strong magnetic fields. *Mon. Not. R. Astron. Soc.* **311**, 555–564 (2000).
20. Heyl, J. & Caiazzo, I. Strongly magnetized sources: QED and X-ray polarization. *Galaxies* **6**, 76 (2018).
21. Radhakrishnan, V. & Cooke, D. J. Magnetic poles and the polarization structure of pulsar radiation. *Astrophys. Lett.* **3**, 225–229 (1969).
22. Poutanen, J. Relativistic rotating vector model for X-ray millisecond pulsars. *Astron. Astrophys.* **641**, A166 (2020).
23. Buchner, J. et al. X-ray spectral modelling of the AGN obscuring region in the CDFS: Bayesian model selection and catalogue. *Astron. Astrophys.* **564**, A125 (2014).
24. Blum, S. & Kraus, U. Analyzing X-ray pulsar profiles: geometry and beam pattern of Hercules X-1. *Astrophys. J.* **529**, 968–977 (2000).
25. Drissen, L., Lamontagne, R., Moffat, A. F. J., Bastien, P. & Seguin, M. Spectroscopic and polarimetric parameters of the runaway WN7 binary system HD 197406: is the secondary an X-ray–quiet black hole? *Astrophys. J.* **304**, 188 (1986).
26. Reynolds, A. P. et al. A new mass estimate for Hercules X-1. *Mon. Not. R. Astron. Soc.* **288**, 43–52 (1997).
27. Leahy, D. A. & Abdallah, M. H. HZ Her: stellar radius from X-ray eclipse observations, evolutionary state, and a new distance. *Astrophys. J.* **793**, 79 (2014).
28. Kolesnikov, D., Shakura, N. & Postnov, K. Evidence for neutron star triaxial free precession in Her X-1 from Fermi/GBM pulse period measurements. *Mon. Not. R. Astron. Soc.* **513**, 3359–3367 (2022).
29. Egonsson, J. & Hakala, P. Discovery of variable optical polarization in Her X-1. *Astron. Astrophys.* **244**, L41–L42 (1991).
30. Shakura, N. I. et al. Observations of Her X-1 in low states during SRG/eROSITA all-sky survey. *Astron. Astrophys.* **648**, A39 (2021).
31. Brown, J. C., McLean, I. S. & Emslie, A. G. Polarisation by Thomson scattering in optically thin stellar envelopes. II. Binary and multiple star envelopes and the determination of binary inclinations. *Astron. Astrophys.* **68**, 415–427 (1978).
32. Kravtsov, V. et al. Orbital variability of the optical linear polarization of the γ-ray binary LS I +61° 303 and new constraints on the orbital parameters. *Astron. Astrophys.* **643**, A170 (2020).
33. Petterson, J. A., Rothschild, R. E. & Gruber, D. E. A model for the 35 day variations in the pulse profile of Hercules X-1. *Astrophys. J.* **378**, 696 (1991).
34. Biryukov, A. & Abolmasov, P. Magnetic angle evolution in accreting neutron stars. *Mon. Not. R. Astron. Soc.* **505**, 1775–1786 (2021).
35. Caiazzo, I. & Heyl, J. Polarization of accreting X-ray pulsars. I. A new model. *Mon. Not. R. Astron. Soc.* **501**, 109–128 (2021).
36. Mönkkönen, J. et al. Constraints on the magnetic field structure in accreting compact objects from aperiodic variability. *Mon. Not. R. Astron. Soc.* **515**, 571–580 (2022).
37. Weisskopf, M. C. et al. The Imaging X-Ray Polarimetry Explorer (IXPE): pre-launch. *J. Astron. Telesc. Instrum. Syst.* **8**, 026002 (2022).
38. Soffitta, P. et al. The instrument of the Imaging X-Ray Polarimetry Explorer. *Astron. J.* **162**, 208 (2021).
39. Baldini, L. et al. Design, construction, and test of the gas pixel detectors for the IXPE mission. *Astropart. Phys.* **133**, 102628 (2021).
40. Kislat, F., Clark, B., Beilicke, M. & Krawczynski, H. Analyzing the data from X-ray polarimeters with Stokes parameters. *Astropart. Phys.* **68**, 45–51 (2015).
41. Baldini, L. et al. ixpeobssim: a simulation and analysis framework for the Imaging X-ray Polarimetry Explorer. SoftwareX 19, 101194 (2022) https://doi.org/10.1016/j.softx.2022.101194
42. Arnaud, K. A. XSPEC: the first ten years. In *Astronomical Data Analysis Software and Systems V* Conference Series Vol. 101 (eds Jacoby, G. H. & Barnes, J.) 17-20 (Astronomical Society of the Pacific, 1996).
43. Rankin, J. et al. An algorithm to calibrate and correct the response to unpolarized radiation of the X-ray polarimeter onboard IXPE. *Astron. J.* **163**, 39 (2022).

44. Di Marco, A. et al. A weighted analysis to improve the X-ray polarization sensitivity of the Imaging X-ray Polarimetry Explorer. *Astron. J.* **163**, 170 (2022).
45. Życki, P. T., Done, C. & Smith, D. A. The 1989 May outburst of the soft X-ray transient GS 2023+338 (V404 Cyg). *Mon. Not. R. Astron. Soc.* **309**, 561–575 (1999).
46. Wit, E., van den Heuvel, E. & Romeijn, J.-W. 'All models are wrong…': an introduction to model uncertainty. *Stat. Neerl.* **66**, 217–236 (2012).
47. Staubert, R., Klochkov, D. & Wilms, J. Updating the orbital ephemeris of Hercules X-1; rate of decay and eccentricity of the orbit. *Astron. Astrophys.* **500**, 883–889 (2009).
48. Lomb, N. R. Least-squares frequency analysis of unequally spaced data. *Astrophys. Space Sci.* **39**, 447–462 (1976).
49. Scargle, J. D. Studies in astronomical time series analysis. II. Statistical aspects of spectral analysis of unevenly spaced data. *Astrophys. J.* **263**, 835–853 (1982).
50. Kuster, M. et al. in *Exploring the Gamma-Ray Universe* Special Publication Vol. 459 (eds Gimenez, A. et al.) 309–312 (ESA, 2001).
51. Wolff, M. T. et al. The NuSTAR X-ray spectrum of Hercules X-1: a radiation-dominated radiative shock. *Astrophys. J.* **831**, 194 (2016).
52. Mushtukov, A. A., Suleimanov, V. F., Tsygankov, S. S. & Poutanen, J. The critical accretion luminosity for magnetized neutron stars. *Mon. Not. R. Astron. Soc.* **447**, 1847–1856 (2015).
53. Staubert, R. et al. Discovery of a flux-related change of the cyclotron line energy in Hercules X-1. *Astron. Astrophys.* **465**, L25–L28 (2007).
54. Zel'dovich, Y. B. & Shakura, N. I. X-ray emission accompanying the accretion of gas by a neutron star. *Sov. Astron.* **13**, 175–183 (1969).
55. Suleimanov, V. F., Poutanen, J. & Werner, K. Accretion heated atmospheres of X-ray bursting neutron stars. *Astron. Astrophys.* **619**, A114 (2018).
56. González-Caniulef, D., Zane, S., Turolla, R. & Wu, K. Atmosphere of strongly magnetized neutron stars heated by particle bombardment. *Mon. Not. R. Astron. Soc.* **483**, 599–613 (2019).
57. Mushtukov, A. A., Suleimanov, V. F., Tsygankov, S. S. & Portegies Zwart, S. Spectrum formation in X-ray pulsars at very low mass accretion rate: Monte Carlo approach. *Mon. Not. R. Astron. Soc.* **503**, 5193–5203 (2021).
58. van Adelsberg, M. & Lai, D. Atmosphere models of magnetized neutron stars: QED effects, radiation spectra and polarization signals. *Mon. Not. R. Astron. Soc.* **373**, 1495–1522 (2006).
59. Suleimanov, V., Potekhin, A. Y. & Werner, K. Models of magnetized neutron star atmospheres: thin atmospheres and partially ionized hydrogen atmospheres with vacuum polarization. *Astron. Astrophys.* **500**, 891–899 (2009).
60. Pavlov, G. G. & Zavlin, V. E. Polarization of thermal X-rays from isolated neutron stars. *Astrophys. J.* **529**, 1011–1018 (2000).

Acknowledgements

This Article is based on observations made by IXPE, a joint US and Italian mission. This research used data products provided by the IXPE Team (MSFC, SSDC, INAF and INFN) and distributed with additional software tools by the High-Energy Astrophysics Science Archive Research Center (HEASARC), at the NASA Goddard Space Flight Center (GSFC). The US contribution is supported by NASA and led and managed by its Marshall Space Flight Center (MSFC), with industry partner Ball Aerospace (contract number NNM15AA18C). The Italian contribution is supported by the Italian Space Agency (Agenzia Spaziale Italiana, ASI) through contract number ASI-OHBI-2017-12-I.0, agreement numbers ASI-INAF-2017-12-H0 and ASI-INFN-2017.13-H0, and its Space Science Data Center (SSDC) and by the Istituto Nazionale di Astrofisica (INAF) and the Istituto Nazionale di Fisica Nucleare (INFN) in Italy. V.D. and V.F.S. acknowledge support from the German Academic Exchange Service (DAAD) under travel grant number 57525212. J.P. and S.S.T. thank the Russian Science Foundation for support under grant number 20-12-00364 and the Academy of Finland for support under grant numbers 333112, 349144, 349373 and 349906. V.F.S. thanks the German Research Foundation (DFG) for grant number WE 1312/53-1. I.C. is a Sherman Fairchild Fellow at Caltech and thanks the Burke Institute at Caltech for supporting her research. A.A.M. acknowledges support from the Netherlands Organization for Scientific Research Veni Fellowship.

Author contributions

V.D. analysed the data and wrote the draft of the manuscript. J.P. led the work of the IXPE Topical Working Group on Accreting Neutron Stars and contributed to modelling the geometrical parameters, the interpretation and the text. S.S.T. produced an independent analysis of the data. V.F.S. led modelling of the polarization from heated atmospheres. A.D.M., F.L.M., F.M. and J.R. provided quick-look analysis of the data and energy scale correction calculation. I.C., J.H., A.A.M., S.Z., R.S. and A.S. contributed to interpretation of the results and writing of the text. M.B. and G.G.P. acted as internal referees of the paper and contributed to interpretation. Other members of the IXPE collaboration contributed to the design of the mission and its science case and planning of the observations. All authors provided input and comments on the manuscript.

Competing interests

The authors declare no competing interests.

Additional information

Extended data is available for this paper at https://doi.org/10.1038/s41550-022-01799-5.

Supplementary information The online version contains supplementary material available at https://doi.org/10.1038/s41550-022-01799-5.

Correspondence and requests for materials should be addressed to Victor Doroshenko or Juri Poutanen.

Peer review information *Nature Astronomy* thanks Hua Feng and Konstantin Postnov for their contribution to the peer review of this work.

Victor Doroshenko[1,50] ✉, Juri Poutanen[2,3,50] ✉, Sergey S. Tsygankov[2,3], Valery F. Suleimanov[1], Matteo Bachetti[4], Ilaria Caiazzo[5], Enrico Costa[6], Alessandro Di Marco[6], Jeremy Heyl[7], Fabio La Monaca[6], Fabio Muleri[6], Alexander A. Mushtukov[8,9], George G. Pavlov[10], Brian D. Ramsey[11], John Rankin[6], Andrea Santangelo[1], Paolo Soffitta[6], Rüdiger Staubert[1], Martin C. Weisskopf[11], Silvia Zane[12], Iván Agudo[13], Lucio A. Antonelli[14,15], Luca Baldini[16,17], Wayne H. Baumgartner[11], Ronaldo Bellazzini[16], Stefano Bianchi[18], Stephen D. Bongiorno[11], Raffaella Bonino[19,20], Alessandro Brez[16], Niccolò Bucciantini[21,22,23], Fiamma Capitanio[6], Simone Castellano[16], Elisabetta Cavazzuti[24], Stefano Ciprini[15,25], Alessandra De Rosa[6], Ettore Del Monte[6], Laura Di Gesu[24], Niccolò Di Lalla[26], Immacolata Donnarumma[24], Michal Dovčiak[27], Steven R. Ehlert[11], Teruaki Enoto[28], Yuri Evangelista[6], Sergio Fabiani[6], Riccardo Ferrazzoli[6], Javier A. Garcia[29], Shuichi Gunji[30], Kiyoshi Hayashida[31,51], Wataru Iwakiri[32], Svetlana G. Jorstad[33,34], Vladimir Karas[27], Takao Kitaguchi[28], Jeffery J. Kolodziejczak[11], Henric Krawczynski[35], Luca Latronico[19], Ioannis Liodakis[36], Simone Maldera[19], Alberto Manfreda[16], Frédéric Marin[37], Andrea Marinucci[24], Alan P. Marscher[33], Herman L. Marshall[38], Giorgio Matt[18], Ikuyuki Mitsuishi[39], Tsunefumi Mizuno[40], Chi-Yung Ng[41], Stephen L. O'Dell[11], Nicola Omodei[26], Chiara Oppedisano[19], Alessandro Papitto[14], Abel L. Peirson[26], Matteo Perri[14,15], Melissa Pesce-Rollins[16], Maura Pilia[4], Andrea Possenti[4], Simonetta Puccetti[15], Ajay Ratheesh[6], Roger W. Romani[26], Carmelo Sgrò[16], Patrick Slane[42], Gloria Spandre[16], Rashid A. Sunyaev[3,43], Toru Tamagawa[28], Fabrizio Tavecchio[44], Roberto Taverna[45], Yuzuru Tawara[39], Allyn F. Tennant[11], Nicolas E. Thomas[11], Francesco Tombesi[25,46,47], Alessio Trois[4], Roberto Turolla[12,45], Jacco Vink[48], Kinwah Wu[12] and Fei Xie[6,49]

[1]Institut für Astronomie und Astrophysik, Universität Tübingen, Tübingen, Germany. [2]Department of Physics and Astronomy, University of Turku, Turku, Finland. [3]Space Research Institute of the Russian Academy of Sciences, Moscow, Russia. [4]INAF Osservatorio Astronomico di Cagliari, Selargius (CA), Italy. [5]TAPIR, Walter Burke Institute for Theoretical Physics, Pasadena, CA, USA. [6]INAF Istituto di Astrofisica e Planetologia Spaziali, Roma, Italy. [7]University of British Columbia, Vancouver, BC, Canada. [8]Astrophysics, Department of Physics, University of Oxford, Oxford, UK. [9]Leiden Observatory, Leiden University, Leiden, The Netherlands. [10]Department of Astronomy and Astrophysics, Pennsylvania State University, University Park, PA, USA. [11]NASA Marshall Space Flight Center, Huntsville, AL, USA. [12]Mullard Space Science Laboratory, University College London, Dorking, Surrey, UK. [13]Instituto de Astrofísica de Andalucía-CSIC, Glorieta de la Astronomía s/n, Granada, Spain. [14]INAF Osservatorio Astronomico di Roma, Monte Porzio Catone (RM), Italy. [15]Space Science Data Center, Agenzia Spaziale Italiana, Roma, Italy. [16]Istituto Nazionale di Fisica Nucleare, Sezione di Pisa, Pisa, Italy. [17]Dipartimento di Fisica, Università di Pisa, Pisa, Italy. [18]Dipartimento di Matematica e Fisica, Università degli Studi Roma Tre, Roma, Italy. [19]Istituto Nazionale di Fisica Nucleare, Sezione di Torino, Torino, Italy. [20]Dipartimento di Fisica, Università degli Studi di Torino, Torino, Italy. [21]INAF Osservatorio Astrofisico di Arcetri, Firenze, Italy. [22]Dipartimento di Fisica e Astronomia, Università degli Studi di Firenze, Sesto Fiorentino (FI), Italy. [23]Istituto Nazionale di Fisica Nucleare, Sezione di Firenze, Sesto Fiorentino (FI), Italy. [24]ASI -Agenzia Spaziale Italiana, Roma, Italy. [25]Istituto Nazionale di Fisica Nucleare, Sezione di Roma Tor Vergata, Roma, Italy. [26]Department of Physics and Kavli Institute for Particle Astrophysics and Cosmology, Stanford University, Stanford, California, USA. [27]Astronomical Institute of the Czech Academy of Sciences, Praha 4, Czech Republic. [28]RIKEN Cluster for Pioneering Research, Wako, Saitama, Japan. [29]California Institute of Technology, Pasadena, CA, USA. [30]Yamagata University, Yamagata-shi, Japan. [31]Osaka University, Suita, Osaka, Japan. [32]Department of Physics, Faculty of Science and Engineering, Chuo University, Bunkyo-ku, Tokyo, Japan. [33]Institute for Astrophysical Research, Boston University, Boston, MA, USA. [34]Department of Astrophysics, St. Petersburg State University, St. Petersburg, Russia. [35]Physics Department and McDonnell Center for the Space Sciences, Washington University in St. Louis, St. Louis, MO, USA. [36]Finnish Centre for Astronomy with ESO, University of Turku, Turku, Finland. [37]Université de Strasbourg, CNRS, Observatoire Astronomique de Strasbourg, Strasbourg, France. [38]MIT Kavli Institute for Astrophysics and Space Research, Massachusetts Institute of Technology, Cambridge, MA, USA. [39]Graduate School of Science, Division of Particle and Astrophysical Science, Nagoya University, Furo-cho, Chikusa-ku, Nagoya, Aichi, Japan. [40]Hiroshima Astrophysical Science Center, Hiroshima University, Hiroshima, Japan. [41]Department of Physics, The University of Hong Kong, Pokfulam, Hong Kong. [42]Center for Astrophysics, Harvard & Smithsonian, Cambridge, MA, USA. [43]Max Planck Institute for Astrophysics, Garching, Germany. [44]INAF Osservatorio Astronomico di Brera, Merate (LC), Italy. [45]Dipartimento di Fisica e Astronomia, Università degli Studi di Padova, Padova, Italy. [46]Dipartimento di Fisica, Università degli Studi di Roma Tor Vergata, Roma, Italy. [47]Department of Astronomy, University of Maryland, College Park, Maryland, USA. [48]Anton Pannekoek Institute for Astronomy & GRAPPA, University of Amsterdam, Amsterdam, The Netherlands. [49]Guangxi Key Laboratory for Relativistic Astrophysics, School of Physical Science and Technology, Guangxi University, Nanning, China. [50]These authors contributed equally: Victor Doroshenko and Juri Poutanen. [51]Deceased: Kiyoshi Hayashida. ✉e-mail: doroshv@astro.uni-tuebingen.de; juri.poutanen@utu.fi

https://doi.org/10.1038/s41550-022-01799-5

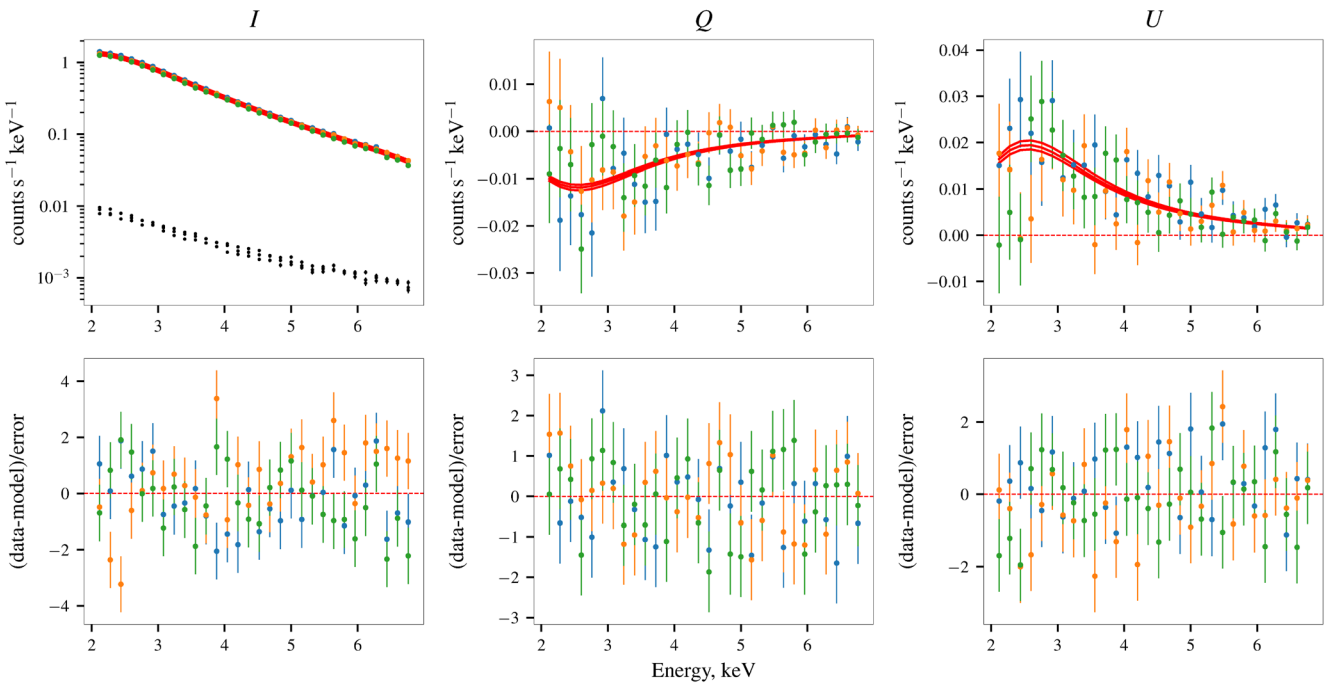

Extended Data Fig. 1 | Observed Stokes spectra of Her X-1. The top row shows spectra of the three Stokes parameters *I*, *Q*, and *U*, while the bottom row shows the residuals to the best-fitting model NTHCOMP for intensity and *polconst* for *Q* and *U*). The results for the three detector units are colour-coded, the black points in the first panel show the estimated background level for each detector.

https://doi.org/10.1038/s41550-022-01799-5

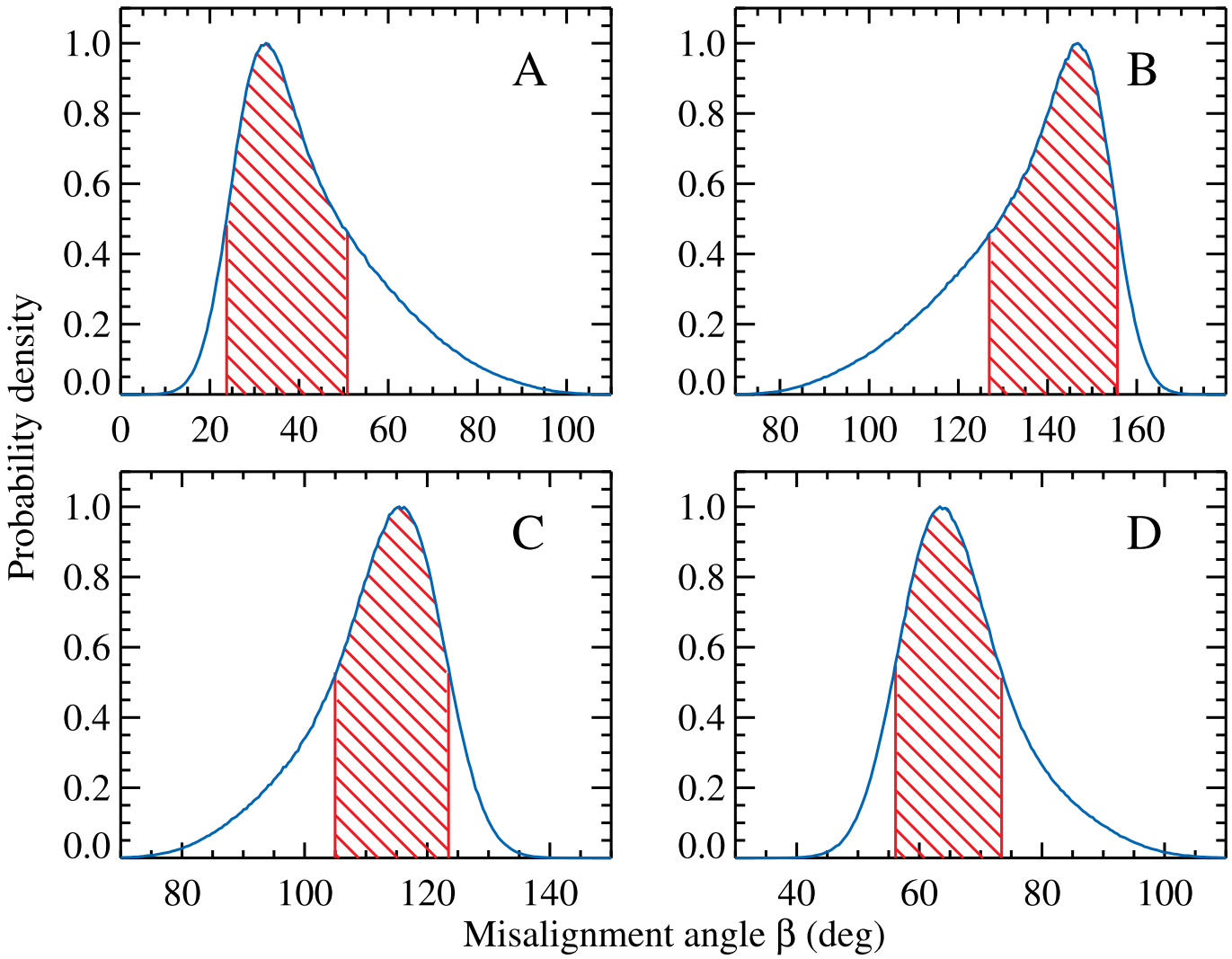

Extended Data Fig. 2 | Probability distribution function for the misalignment angle. The distribution normalized to the peak value is shown for the misalignment angle between the pulsar and the orbital angular momenta. The red hatched region corresponds to the 68% confidence interval (that is between 16th and 84th percentiles of the posterior probability distribution). Four panels correspond to four different cases for the choice of χ_p: **(A)** $\chi_p = \chi_{p,*} = 56.9° \pm 1.6°$; **(B)** $\chi_p = \chi_{p,*} + 180°$; **(C)** $\chi_p = \chi_{p,*} + 90°$; **(D)** $\chi_p = \chi_{p,*} - 90°$. Here we take $\chi_{orb} = \chi_{orb,*} = 28.9° \pm 5.9°$.

nature astronomy

Article

https://doi.org/10.1038/s41550-022-01799-5

Determination of X-ray pulsar geometry with IXPE polarimetry

In the format provided by the authors and unedited

1 Supplementary Tables

Supplementary Table 1 Average X-ray polarization of Her X-1. Pulse-phase averaged spectro-polarimetric fit results. The Stokes parameters spectra are modelled with `nthcomp` (I), and either constant polarization (`polconst`) model or model where a power-law type dependence is allowed for the PD and PA (`polpow`) for Q and U spectra. The uncertainties are reported at the 1σ confidence level based on `mcmc` chains obtained as described in the text.

Parameter	`polpow`	`polconst`
$\mathrm{PD}_{1\,\mathrm{keV}}$ (%)	$4.7^{+1.5}_{-1.2}$	8.6 ± 0.5
Γ_{PD}	-0.46 ± 0.20	
$\mathrm{PA}_{1\,\mathrm{keV}}$, deg	64^{+10}_{-9}	$60.2^{+1.8}_{-1.7}$
Γ_{PA}	0.04 ± 0.10	
$kT_{\mathrm{e,comp}}$, keV	$6.6^{+2.5}_{-1.4}$	$7.4^{+3.5}_{-2.0}$
$kT_{\mathrm{bb,comp}}$, keV	$0.349^{+0.015}_{-0.018}$	$0.345^{+0.017}_{-0.024}$
Γ_{comp}	$1.28^{+0.035}_{-0.05}$	$1.26^{+0.05}_{-0.06}$
A_{comp}	$0.0984^{+0.0033}_{-0.0027}$	$0.0990^{+0.004}_{-0.0028}$
C_{DU2}	0.9767 ± 0.0026	$0.9766^{+0.0026}_{-0.0025}$
C_{DU3}	$0.8923^{+0.0024}_{-0.0025}$	0.8922 ± 0.0024
χ^2/d.o.f./BIC	593.4/539/656.5	598.2/541/648.7

Supplementary Table 2 Pulse-phase resolved X-ray polarization of Her X-1. Pulse-phase resolved spectro-polarimetric fit results for the `nthcomp` continuum flux and constant polarization `polconst` models. Uncertainties are reported at 1σ confidence level based on `mcmc` chains obtained as described in the text.

Phase	PD, %	PA, deg	Γ_{comp}	$A_{\mathrm{comp}}/10^{-2}$	χ^2/d.o.f.
0.00–0.14	12.4 ± 1.9	46 ± 4	1.259 ± 0.007	4.56 ± 0.05	560.8/543
0.14–0.29	9.0 ± 1.7	50 ± 5	1.263 ± 0.006	5.88 ± 0.06	580.6/543
0.29–0.43	14.0 ± 1.8	47 ± 4	1.329 ± 0.008	5.96 ± 0.07	552.7/543
0.43–0.57	15.5 ± 1.7	56 ± 3	1.268 ± 0.006	5.83 ± 0.06	563.0/543
0.57–0.71	7.1 ± 1.0	78 ± 4	1.272 ± 0.004	16.06 ± 0.10	600.6/543
0.71–0.86	10.7 ± 1.1	71 ± 3	1.344 ± 0.004	17.44 ± 0.11	617.2/543
0.86–1.00	5.5 ± 1.2	48 ± 6	1.286 ± 0.004	11.99 ± 0.08	676.5/543

Supplementary Table 3 Evolution of X-ray polarization of Her X-1. Time-resolved spin-phase averaged spectro-polarimetric fit results for `nthcomp` continuum flux and constant polarization `polconst` models. Uncertainties are reported at the 1σ confidence level based on the `mcmc` chains obtained as described in the text.

Time interval, MJD	PD,%	PA, deg	$\Gamma_{\rm comp}$	$A_{\rm comp}$	χ^2/dof
59628.53–59628.84	14.2 ± 2.4	66 ± 5	1.113 ± 0.003	0.0313 ± 0.0004	606.3/543
59629.07–59629.39	11.9 ± 1.8	66 ± 4	1.249 ± 0.006	0.0716 ± 0.0008	529.6/543
59629.86–59630.47	7.0 ± 1.2	61 ± 5	1.281 ± 0.004	0.0982 ± 0.0007	525.9/543
59630.45–59631.06	6.9 ± 1.0	60 ± 4	1.282 ± 0.004	0.1101 ± 0.0007	607.2/543
59631.49–59631.66	7.7 ± 2.0	54 ± 7	1.288 ± 0.007	0.1187 ± 0.0013	577.5/543
59633.19–59633.82	9.8 ± 1.1	59 ± 3	1.351 ± 0.005	0.1169 ± 0.0008	588.1/543
59633.75–59634.33	9.3 ± 1.2	58 ± 4	1.337 ± 0.005	0.1066 ± 0.0007	571.8/543

Supplementary Table 4 Optical polarization of Her X-1. Fourier coefficients and their errors obtained by re-fitting the optical polarimetric data from [25] and Eq. 9

Stokes	q_0/u_0	q_1/u_1	q_2/u_2	q_3/u_3	$q_4/\ u_4$	χ^2/dof
q	0.015 ± 0.012	0.005 ± 0.012	0.002 ± 0.020	-0.080 ± 0.018	-0.034 ± 0.018	17.0/11
u	0.102 ± 0.016	0.006 ± 0.016	0.035 ± 0.026	-0.118 ± 0.024	0.040 ± 0.023	12.7/11

Supplementary Table 5 Misalignment angle. Misalignment angle β between the pulsar and orbital spins is computed for the four possible cases identified by letters A–D of the pulsar spin orientation. Here we assume $\chi_{\rm orb} = \chi_{\rm orb,*}$. The errors correspond to the 68% confidence level. The probability distributions for the cases A–D are shown in Extended Data Figure 2. If the orbital spin position angle differs by 180° from $\chi_{\rm orb,*}$, the resulting constraints on β are the same if $\chi_{\rm p}$ is also rotated by 180°.

	O-mode polarization		X-mode polarization	
Case	A	B	C	D
$\chi_{\rm p}$ (deg)	$\chi_{\rm p,*} = 56.9 \pm 1.6$	$\chi_{\rm p,*} \pm 180°$	$\chi_{\rm p,*} + 90°$	$\chi_{\rm p,*} - 90°$
β (deg)	33^{+18}_{-9}	147^{+9}_{-20}	115^{+8}_{-10}	63^{+10}_{-7}

2 Supplementary Figures

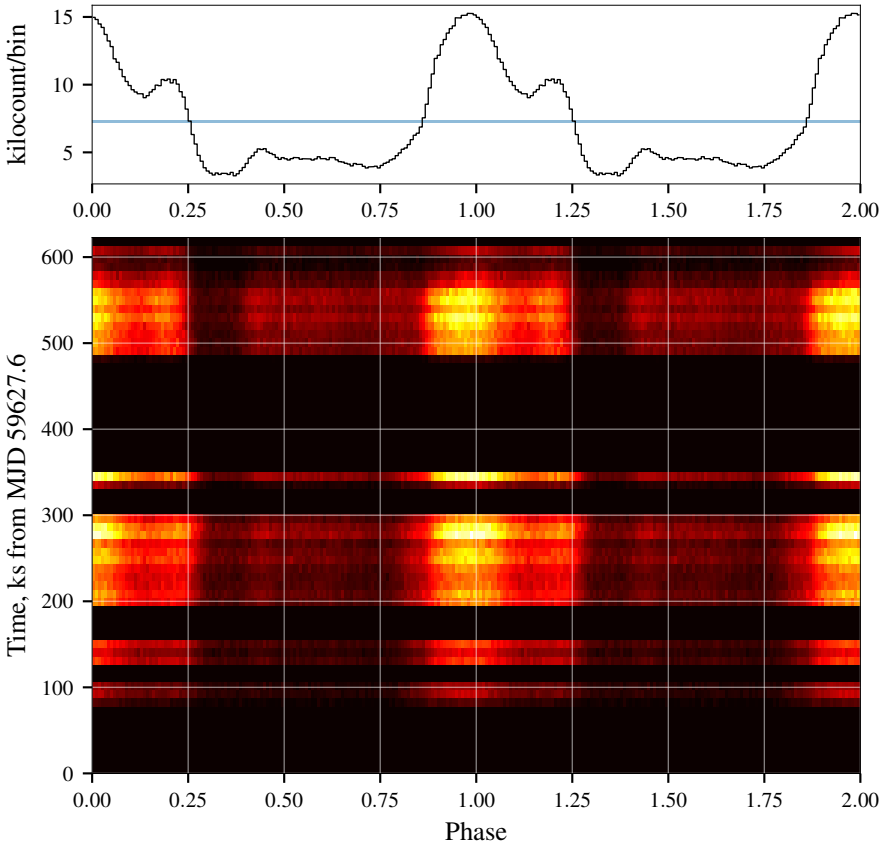

Supplementary Figure 1 Variation of the pulse profile of Her X-1 over the observation. Top panel shows the observed pulse profile averaged over entire observation (128 phase bins). The horizontal line indicates average count-rate. The bottom panel shows the phaseogram, i.e. colour-coded pulse profiles of individual observational segments folded with the same period, for the final timing solution obtained as discussed in the text. The phaseogram illustrates the lack of appreciable phase shifts (i.e. accuracy of the timing solution) and stability of the pulse profile shape during the observation.

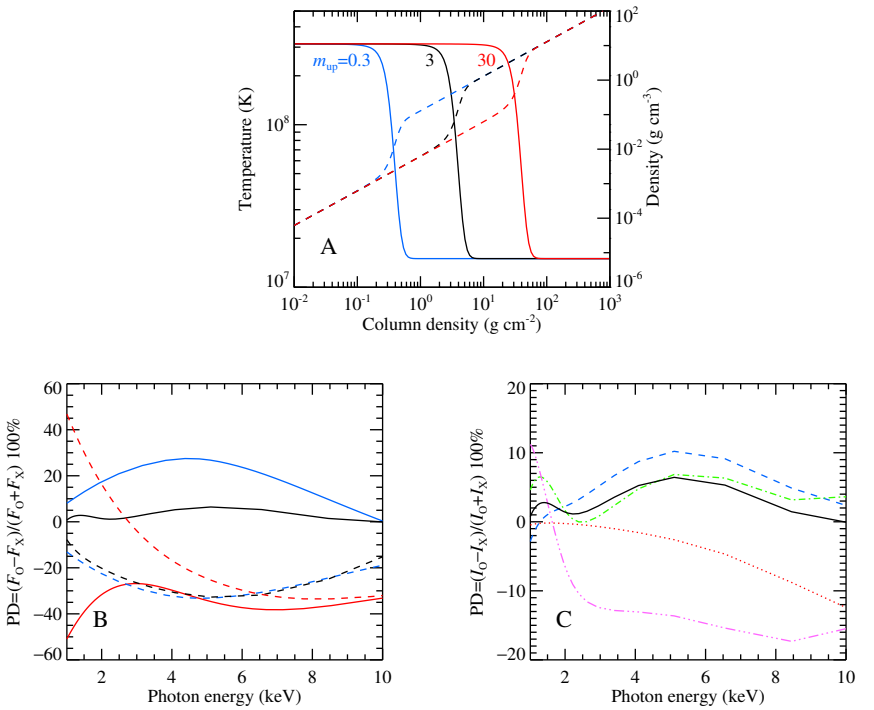

Supplementary Figure 2 Structure of the heated layer and the emergent polarization. (A) Temperature dependencies on column density (solid curves, left axis) and the corresponding density dependencies (dashed curves, right axis) for three different mass column densities of the heated layer $m_{\rm up} = 0.3, 3$, and 30 g cm^{-2} are shown with blue, black and red colours. **(B)** PD of the emergent angle-integrated flux as a function of the photon energy in the IXPE energy band for the three models with the mode conversion taken into account (solid curves) and without the mode conversion (dashed curves). **(C)** PD of the emergent radiation intensity as a function of the photon energy for the model $m_{\rm up} = 3$ g cm^{-2} with the mode conversion taken into account. Coloured lines correspond to the zenith angles of 10° (red dotted), 30° (blue dashed), 60° (green dot-dashed), and 81° (pink triple-dot-dashed), while the black solid line corresponds to the PD of the flux.

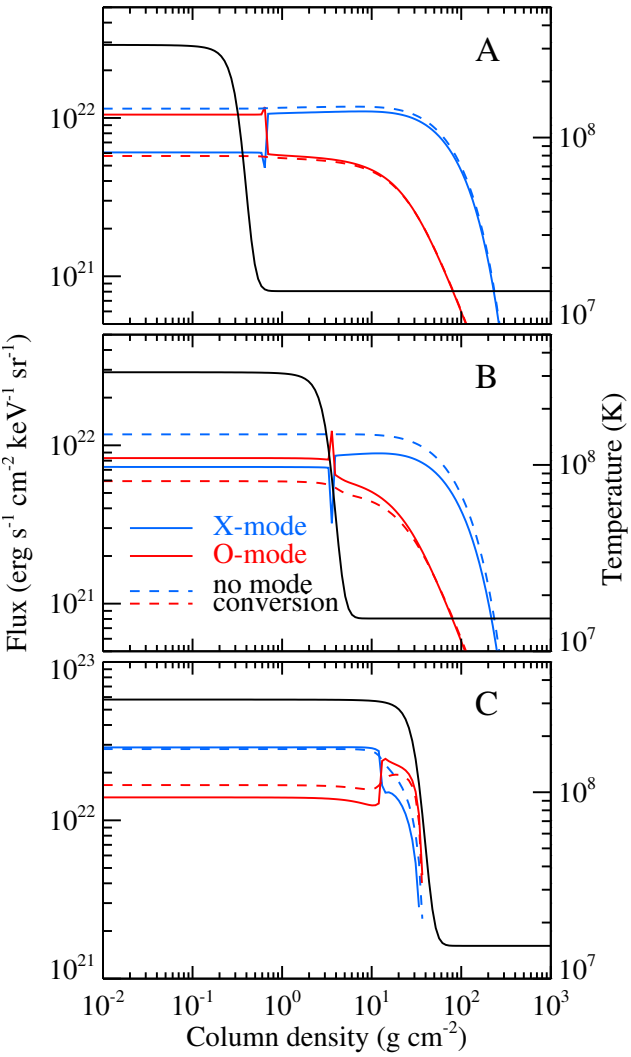

Supplementary Figure 3 Flux emergent from the heated layer in two polarization modes. Distributions of the fluxes in two polarization modes, X and O, as a function of the column density at photon energy of 5.1 keV are shown with blue and red curves for the three models with $m_{\rm up} = 0.3, 3$, and 30 g cm^{-2} in panels **(A)**, **(B)**, and **(C)**, respectively. Models with and without mode conversion at the vacuum resonance are shown with the solid and dashed curves, respectively. The corresponding temperature distributions are shown with the black curves (right axes).